UC Office of the President
Recent Work

Title

Transport of kJ-laser-driven relativistic electron beams in cold and shock-heated vitreous carbon and diamond

Permalink

Journal

ISSN

Authors

Bailly-Grandvaux, M
Kim, J
Krauland, C M
et al.

Publication Date

DOI

Peer reviewed

PAPER • OPEN ACCESS

Transport of kJ-laser-driven relativistic electron beams in cold and shock-heated vitreous carbon and diamond

To cite this article: M Bailly-Grandvaux *et al* 2020 *New J. Phys.* **22** 033031

View the article online for updates and enhancements.

New Journal of Physics

The open access journal at the forefront of physics

Deutsche Physikalische Gesellschaft **DPG**

IOP Institute of Physics

Published in partnership with: Deutsche Physikalische Gesellschaft and the Institute of Physics

CrossMark

OPEN ACCESS

PAPER

Transport of kJ-laser-driven relativistic electron beams in cold and shock-heated vitreous carbon and diamond

M Bailly-Grandvaux[1,8] , J Kim[1,8] , C M Krauland[2,8] , S Zhang[1], M Dozières[1] , M S Wei[3] , W Theobald[3], P E Grabowski[4], J J Santos[5] , Ph Nicolaï[5], P McKenna[6] , M P Desjarlais[7] and F N Beg[1]

1   Center for Energy Research, University of California San Diego, La Jolla, CA, 92093, United States of America
2   General Atomics, San Diego, CA, 92121, United States of America
3   Laboratory for Laser Energetics, Rochester, NY, 14623, United States of America
4   Lawrence Livermore National Laboratory, Livermore, CA, 94550, United States of America
5   Univ. Bordeaux, CNRS, CEA, CELIA (Centre Lasers Intenses et Applications), UMR 5107, F-33405, Talence, France
6   SUPA, Department of Physics, University of Strathclyde, Glasgow, United Kingdom
7   Sandia National Laboratories, Albuquerque, NM, 87185, United States of America
8   These authors contributed equally to this work.

E-mail: mbaillygrandvaux@ucsd.edu

Abstract

We report experimental results on relativistic electron beam (REB) transport in a set of cold and shock-heated carbon samples using the high-intensity kilojoule-class OMEGA EP laser. The REB energy distribution and transport were diagnosed using an electron spectrometer and x-ray fluorescence measurements from a Cu tracer buried at the rear side of the samples. The measured rear REB density shows brighter and narrower signals when the targets were shock-heated. Hybrid PIC simulations using advanced resistivity models in the target warm-dense-matter (WDM) conditions confirm this observation. We show that the resistivity response of the media, which governs the self-generated resistive fields, is of paramount importance to understand and correctly predict the REB transport.

1. Introduction

When an intense laser pulse interacts with a dense (opaque) target, a high-current relativistic electron beam (REB) is generated and driven into the target. As the beam propagates, a significant fraction of the laser energy is coupled into the target's depth [1–5]. The transport of intense current (>1 MA) of REB into dense matter is of critical importance for various applications such as secondary sources of energetic particles [6] and radiation [7, 8], and for isochoric heating of matter to temperatures relevant to the study of structural and dynamic properties of warm dense matter or high-energy-density (HED) matter [9–14]. This is also of interest in planetary science [15–17], astrophysics [18, 19], or for the development of high-gain inertial confinement fusion schemes [20–24]. The electron transport through solid density is however impaired by the resistive and collisional energy losses [25–28] and by the intrinsic large divergence of the REB [29–33]. For the electron fast ignition (FI) scheme [34], at the very end of the compression, during stagnation time, an intense laser pulse is focused to accelerate a population of fast electrons to deposit their energy into the dense core, thereby heating the compressed core to fusion temperatures. The REB needs to propagate over a 100 μm long shock-heated medium from the laser-absorption region up to the dense core [35]. It is therefore of significant importance to understand the underlying physics of REB transport through the WDM region, and control its propagation to a small radius.

Several methods to guide the REB along its propagation have been proposed. Most of those rely on the collimating effect of MeV electrons via either self-generated [20, 36–39] or imposed magnetic fields on the kilo-Tesla (kT) range [40, 41]. For instance, studies have pointed out that materials with an atomic number greater

than Al, that have high heat capacity and ionization level, can yield stable resistive collimation fields over the REB time scale and therefore enhance its collimation [42–44]. While those materials can be used for the cone tip foil in a cone-shell fast-ignition (FI) design [45–47], the majority of the ∼100 μm-length REB propagation is made through compressed plastic or silicon (shell) and DT (fuel). Besides, if the propagation length is more than a few tens of microns, the higher Z materials would yield strong collisional losses of the REB. Even though some experiments focused on exploring REB transport in samples of initial high resistivity while relatively low density [48, 49], they have been done with initially cold solid targets, where the resistivity is far from that in FI conditions. A few among them explored conditions linked to the FI scenario where the REB propagates into shock-heated warm dense matter in Al [50, 51] or plastic [52–54]. However, ⩽100 J and ⩽1 ps lasers were used, yielded electron beam energy also far from that in FI conditions. While these studies have yielded a valuable new understanding of REB transport, a demonstration for FI applications with a more energetic driver is warranted.

The REB divergence depends strongly on the beam current density and target resistivity, the latter varying by several orders of magnitude depending on the initial condition of the target. Nevertheless, calculation of the target resistivity in the WDM regime is very challenging and models can easily disagree by a factor 5. It is therefore warranted to perform further experimental characterization and benchmark resistivity models for accurate numerical predictions.

We performed REB transport experiments on the kJ-class OMEGA-EP laser facility using a set of cold and shock-heated carbon samples. We observed that in the shock-heated materials, the REB transport can be efficiently guided through the sample. By implementing dynamic resistivity tables in our REB transport simulations, we are able to validate experimental data on REB transport. This work shows that in the shock-heated targets, the divergence of the electron beam can be reduced with respect to the initially cold and solid density carbon target due to a stable growth of resistive collimation.
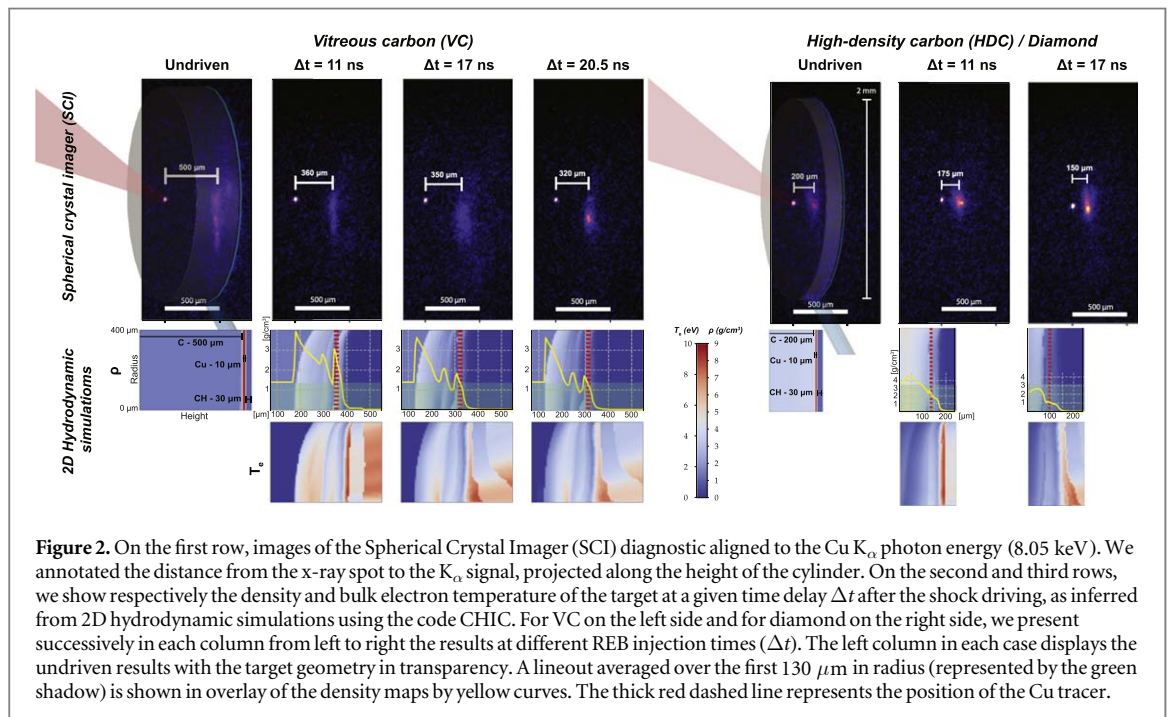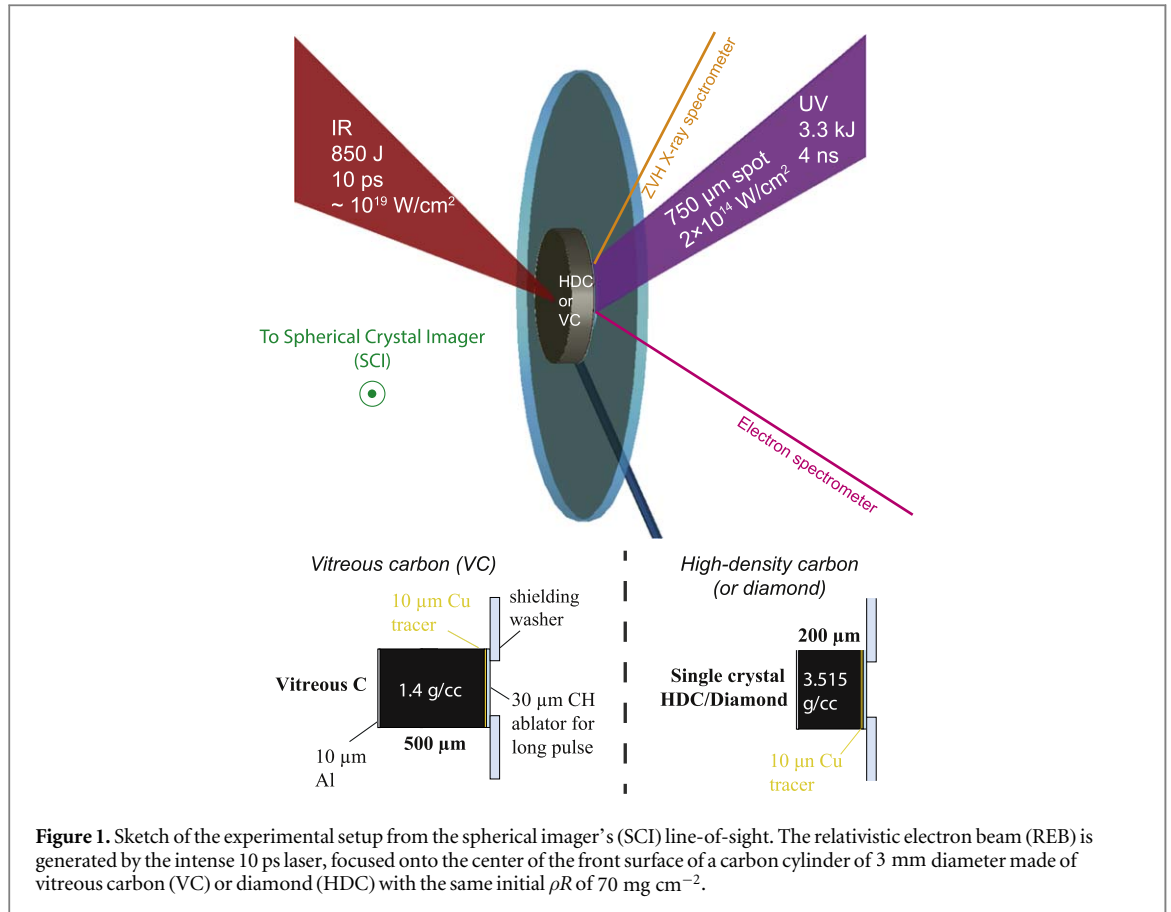
2. Results

2.1. Experimental setup

The experiments were conducted at the OMEGA EP laser facility with a dual laser beam configuration in planar geometry: a high-energy UV long-pulse beam equipped with a distributed phase plate (DPP) for beam smoothing (LP: 4 ns, 3.3 kJ, 2×10^{14} W cm^{-2}) was focused onto the rear surface of the target coated with 30 μm CH over a focal spot of 750 μm FWHM and launched a shock in the carbon sample; the high-intensity EP short-pulse beam (SP: 10 ps, 850 J, $\sim 10^{19}$ W cm^{-2}) was focused on the opposite side of the target and generated a REB in the shock-heated target at varying delays Δt with respect to the LP-laser. The setup is sketched in figure 1.

The REB transport targets were 3 mm diameter with 500 μm or 200 μm length, respectively for vitreous carbon (VC) or diamond (HDC) materials, leading to a similar ρR of 70 mg cm^{-2}. To investigate the REB transport in different conditions of background across the WDM regime, we varied the time delay Δt between shock driving and REB generation from 11 to 20.5 ns. REB patterns were investigated by imaging the K$_\alpha$ emission from a buried 10 μm thick Cu layer at the cylinder's rear side. Emission lines between 7 to 10 keV were also recorded with an absolutely calibrated x-ray spectrometer (ZVH) [55], with a spectral resolution $E/\Delta E \approx 100$. Escaping electrons' energy distribution was measured from the target rear using an electron spectrometer with energy range from ∼40 keV to ∼40 MeV [56]. Over the fast REB transport time (∼100 ps), the target is considered static: the hydrodynamic conditions evolve over ns timescales and can therefore be considered as background conditions for the REB transport at the different probing times Δt.

2.2. Experimental results

The evolution of the transport-target density and temperature prior to the REB injection were predicted by 2D hydrodynamic simulations using the code CHIC. The results showing background density and bulk electron temperature are presented in the two bottom rows of figure 2. We present in each successive column the results at the REB injection delays explored during the experiment, both for vitreous carbon and diamond samples. Note that the density range is from 1 to 10 g cm^{-3} and the temperatures from 1 to 10 eV indicating the WDM initial conditions of the transport target. The background electron temperature upon injecting the REB remains below 100 eV for ∼ ps, specifically at the edges of the REB where the resistive gradient field is developing, further justifying the importance of carefully computing the resistivity in WDM for accurate prediction of the REB transport [49, 54]. Further details on the hydrodynamic modeling are given in the *Methods* section.

In the first row of figure 2, we present the results of the Spherical Crystal Imager (SCI) [57], which records the spatial pattern of K$_\alpha$ fluorescence (8.05 keV) emitted when the fast electron beam impinges the Cu layer buried at the back of the target. In the figure, the target geometry is overlapped in transparency for the undriven cases (when the target was not shocked by the LP UV beams). Two signals are identified: (i) a bright spot is emitted at

Figure 1. Sketch of the experimental setup from the spherical imager's (SCI) line-of-sight. The relativistic electron beam (REB) is generated by the intense 10 ps laser, focused onto the center of the front surface of a carbon cylinder of 3 mm diameter made of vitreous carbon (VC) or diamond (HDC) with the same initial ρR of 70 mg cm^{-2}.

Figure 2. On the first row, images of the Spherical Crystal Imager (SCI) diagnostic aligned to the Cu K$_\alpha$ photon energy (8.05 keV). We annotated the distance from the x-ray spot to the K$_\alpha$ signal, projected along the height of the cylinder. On the second and third rows, we show respectively the density and bulk electron temperature of the target at a given time delay Δt after the shock driving, as inferred from 2D hydrodynamic simulations using the code CHIC. For VC on the left side and for diamond on the right side, we present successively in each column from left to right the results at different REB injection times (Δt). The left column in each case displays the undriven results with the target geometry in transparency. A lineout averaged over the first 130 μm in radius (represented by the green shadow) is shown in overlay of the density maps by yellow curves. The thick red dashed line represents the position of the Cu tracer.

the interaction point between the SP beam and the target front surface, which corresponds to the bremsstrahlung emission at 8.05 ± 0.01 keV from the focal spot area; (ii) a signal within a broad background appears at the rear side of the target, where the Cu tracer is located. This emission corresponds to the K$_\alpha$ fluorescence in the Cu tracer and is a signature of the REB spatial pattern at the rear side of the target. The broad emission background originates from the electron refluxing occurring at the sharp rear interface of the undriven targets. This emission disappears for the LP driven cases due to the plasma expansion of the rear surface which
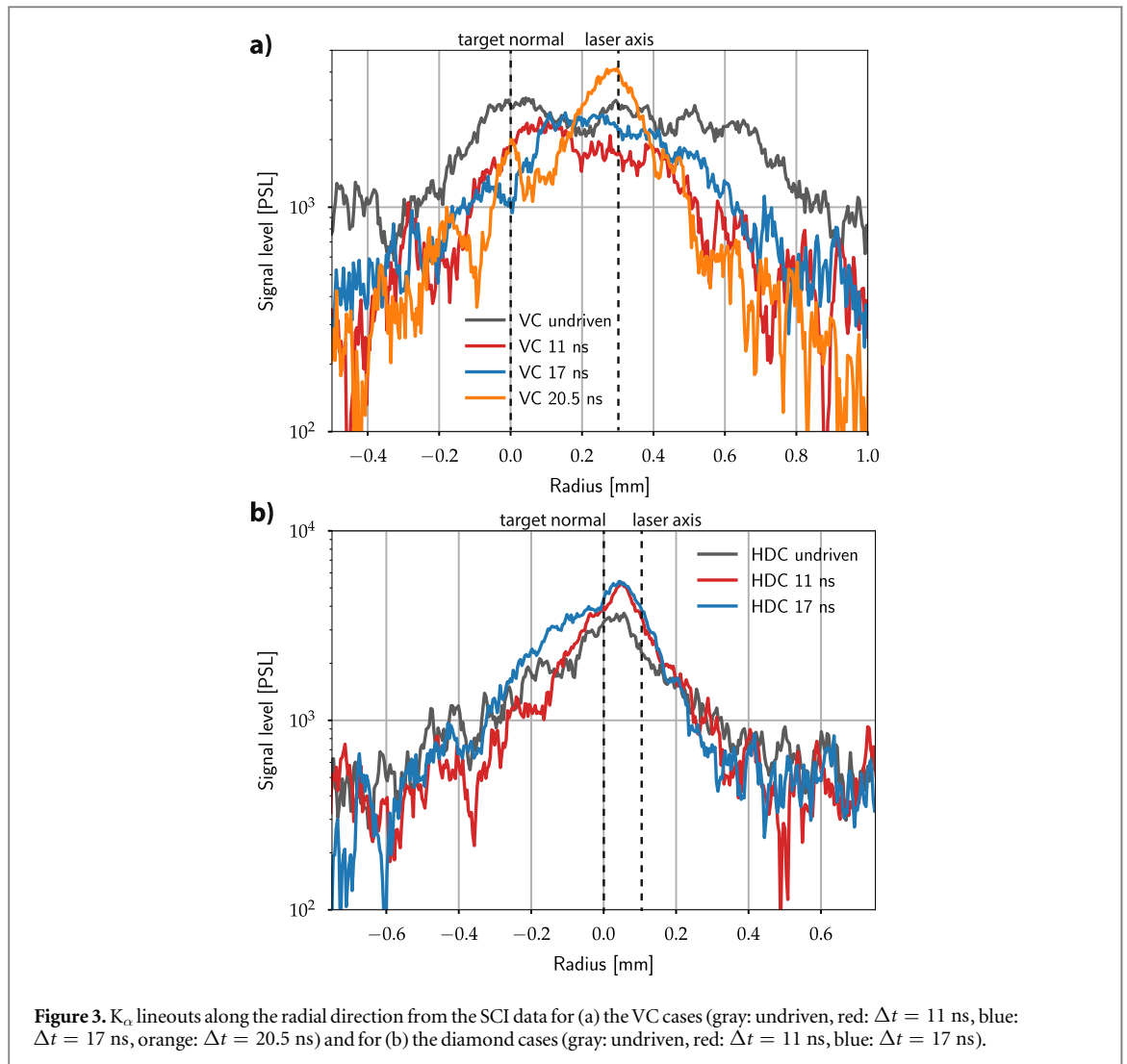
Figure 3. K_α lineouts along the radial direction from the SCI data for (a) the VC cases (gray: undriven, red: $\Delta t = 11$ ns, blue: $\Delta t = 17$ ns, orange: $\Delta t = 20.5$ ns) and for (b) the diamond cases (gray: undriven, red: $\Delta t = 11$ ns, blue: $\Delta t = 17$ ns).

terminates the refluxing [58]. Note that the electron refluxing persists over a longer time than the time required for a first pass of the REB through the Cu tracer and can be regarded as a background noise for this time-integrated diagnostic. Figure 3 depicts the corresponding lineouts along the radial direction of the K_α emission from the SCI images, on the top graph (a) for the VC cases and on the bottom graph (b) for the diamond cases. When the target is shock-heated (for increasing delays Δt), in addition to the large decrease of the background, the brighter part of the signal—indicating the first-pass REB density in the Cu layer—is getting narrower and more intense. It is very clear for $\Delta t = 20.5$ ns with VC where the FWHM of the emission decreases from 850 μm to 310 μm and the signal peak gets stronger by 35% compared to the undriven case. Although for the diamond cases the signal is already narrow for the undriven case, it also evidences stronger focusing for driven cases. One could note in figure 2 that the position of the brightest spot of the signal for driven HDC, also seen for $\Delta t = 20.5$ ns for VC, roughly matches the direction of the laser. It can be inferred that it corresponds to the high-energy component of the REB which tends to follow the laser direction, while the low-energy part tends to follow the target normal direction [50, 59]. The contributions will eventually sum up and this explains why the signal is elongated vertically between the target normal and laser direction intersection points on the Cu tracer, resulting in a peak offset towards this direction in the corresponding lineouts shown in figure 3.

On the SCI images of figure 2, we see that the depth of the K_α signal along the cylinder height (i.e. the position of the Cu tracer) decreases while the target gets compressed from 500 μm for the undriven VC case to $\approx$360 μm for $\Delta t = 11$ ns, $\approx$350 μm for $\Delta t = 17$ ns and $\approx$320 μm for $\Delta t = 20.5$ ns. Similarly, for the diamond cases the depth of the Cu tracer is reduced from 200 μm for the undriven case to $\approx$175 μm for $\Delta t = 11$ ns and $\approx$150 μm for $\Delta t = 17$ ns. The distances listed above between the x-ray point and the K_α signal are annotated on each SCI images. The Cu tracer position from the hydrodynamic simulation is also marked along the density 1D profiles (yellow curves) by a thick dashed red line. For vitreous carbon, the positions of the Cu tracer are consistent with the hydrodynamic simulations by $\pm$10 μm, except for $\Delta t = 17$ ns for which the simulation underestimate the distance by $\approx$30 μm. However, the diamond cases consistently suggest an offset of $\approx$50 μm

with the simulations. This discrepancy could be due to the equation-of-state used in the hydrodynamic code for diamond, which may require a better qualification.

In what follows we will focus on the VC cases that will be further compared with REB transport simulations. Indeed, in addition to the compression offset observed between the data and the hydrodynamic simulations for diamond, the diamond cases present two additional difficulties for the modeling: (i) the shock already broke out at $\Delta t = 11$ ns, therefore inducing plasma expansion on the front surface which complicates the REB source modeling; (ii) in the WDM regime, the modeling of diamond target resistivities is challenged by the additional difficulty of accounting for the lattice structure effects. The diamond cases will consequently be the object of a further article building upon the validation of our REB modeling for the VC cases.

K_α radiation is generated by inner-shell ionization of the Cu atoms and successive radiative decay of the atom in the excited state. In a simple manner, the number of K_α photons emitted in the process can be written as:

$$n_{K\alpha} = n_{e_{\mathrm{fast}}^-} \eta_K \int \sigma(E) f(E) \, \mathrm{d}E, \tag{1}$$

where $n_{e_{\mathrm{fast}}^-}$ is the number density of fast electrons, $\sigma(E)$ the total cross-section of K-shell ionization as a function of the fast electron energy, $f(E)$ the fast electron energy distribution normalized to unity and η_K is the fluorescence probability. In the approximation that the energy distribution of the fast electrons remains the same, the K_α yield therefore only depends on the fast electron density and material properties (temperature and density). An atomic code, such as FLYCHK, can calculate the K_α emission for differing target bulk densities and temperatures by injecting a hot component to simulate the excitation from fast electrons. In figure 4(a) we present the results from the Zinc Von Hamos (ZVH) time-integrated spectrometer, recording the x-ray emission from 7.8 to 9.2 keV with a resolution of $E/\Delta E \approx 100$. At respectively 8.05 keV, 8.3 keV and 8.9 keV, we identify the Cu K_α, He_α and K_β lines. The FLYCK calculations show that at temperatures >150 eV, the Cu K_α line disappears (it decays from 100 eV), and the He_α line emerges. The hot electron component is introduced by a second Maxwellian distribution with a temperature of 1 MeV and its fraction to the total electron density will be adjusted and discussed further. To estimate the Cu emission for the different delays Δt, the Cu density profile is extracted from the hydrodynamic simulations and used as an input in FLYCHK. The Cu density is 8.96 g cm^{-3} (solid density), 1.6 g cm^{-3}, 1.1 g cm^{-3} and 0.8 g cm^{-3}, respectively for the undriven, $\Delta t = 11$ ns, $\Delta t = 17$ ns and $\Delta t = 20.5$ ns cases. The density decreases with the rear target surface expansion and the Cu length consequently increases from 10 μm to 43 μm, 65 μm and 86 μm, respectively for $\Delta t = 11$ ns, $\Delta t = 17$ ns and $\Delta t = 20.5$ ns. The Cu density strongly influence the K_α and K_β lines intensities with a nonlinear cross-section varying by three orders of magnitude for Cu between 0.8 g cm^{-3} and 8.96 g cm^{-3}, according to FLYCHK. It is therefore critical to be accounted for in order to estimate the corresponding fast electron density (or fast electron fraction) from the measured yields.

As the ZVH diagnostic is time-integrated, we simulated two different bulk temperatures: (i) a temperature for the K_α and K_β emission emitted when the target is 'cold' and (ii) a temperature for the He_α line, emitted later and resulting from the heating and ionization of the target by the REB. In figure 4(b), we present the results from FLYCHK at two bulk temperatures, 10 eV (solid lines) for the K_α and K_β lines and at 400 eV (dotted lines) for the He_α, taking into account the Cu length and density from the hydrodynamic simulations for each delay Δt. The relative intensities of the He_α between the different delays are reproduced for the same bulk temperature of 400 eV. This temperature is where the He_α cross-section is maximum and peaks at 8.3 keV, as recorded in the ZVH spectra. This hot line is rather weak for the undriven case (gray line) in figure 4(a), suggesting that the target does not get as hot and conveys the idea of a poor REB energy density coupling in this case. The REB current density is high at the center of the beam: it is where the hottest emission of the Cu will be emitted. While, for a focused beam, the tightly deposited REB energy can significantly increase the peak temperature, the energy density of a defocused REB beam (as captured by the Cu K_α emission in SCI for the undriven case) is more diluted and the peak temperature is expected to be much lower. For the focused cases, in order to emit the He_α line, the Cu is expected to reach >150 eV temperature after the electron energy deposition and heat transfer to the Cu ions. The increased temperature of the Cu between the undriven and driven case is confirmed by our PIC simulations further presented in the next section, from which the Cu electron temperature amounts to a maximum of 80 eV for the undriven case and 600–800 eV for the driven cases. Still, the He_α is self-emitted several picoseconds after the REB first pass and does not directly correlate to the fast electron density. On the contrary, the K_α and K_β lines are generated by the REB when the Cu is still cold, and thus are a signature of the fast electron density, as discussed before for the SCI. According to FLYCHK, the ratio of K_α and K_β lines of $\sim$6–7 and the position of the K_β line at 8.9 keV constrain the bulk electron temperature between 10 eV and 20 eV. Indeed, the K_β lines vanish for temperature >20 eV. Assuming that the density of the Cu remains the same between the $K_{\alpha,\beta}$ and He_α emissions (the Cu most probably does not have time to expand), we could reproduce the relative magnitude of the K_α lines at different delays and their ratio to He_α lines by adjusting the hot component fraction in the FLYCHK calculations. The corresponding hot electron fraction and hot electron densities (hot electron fraction $\times$ bulk electron density) for the solid curves of figure 4(b) are shown in
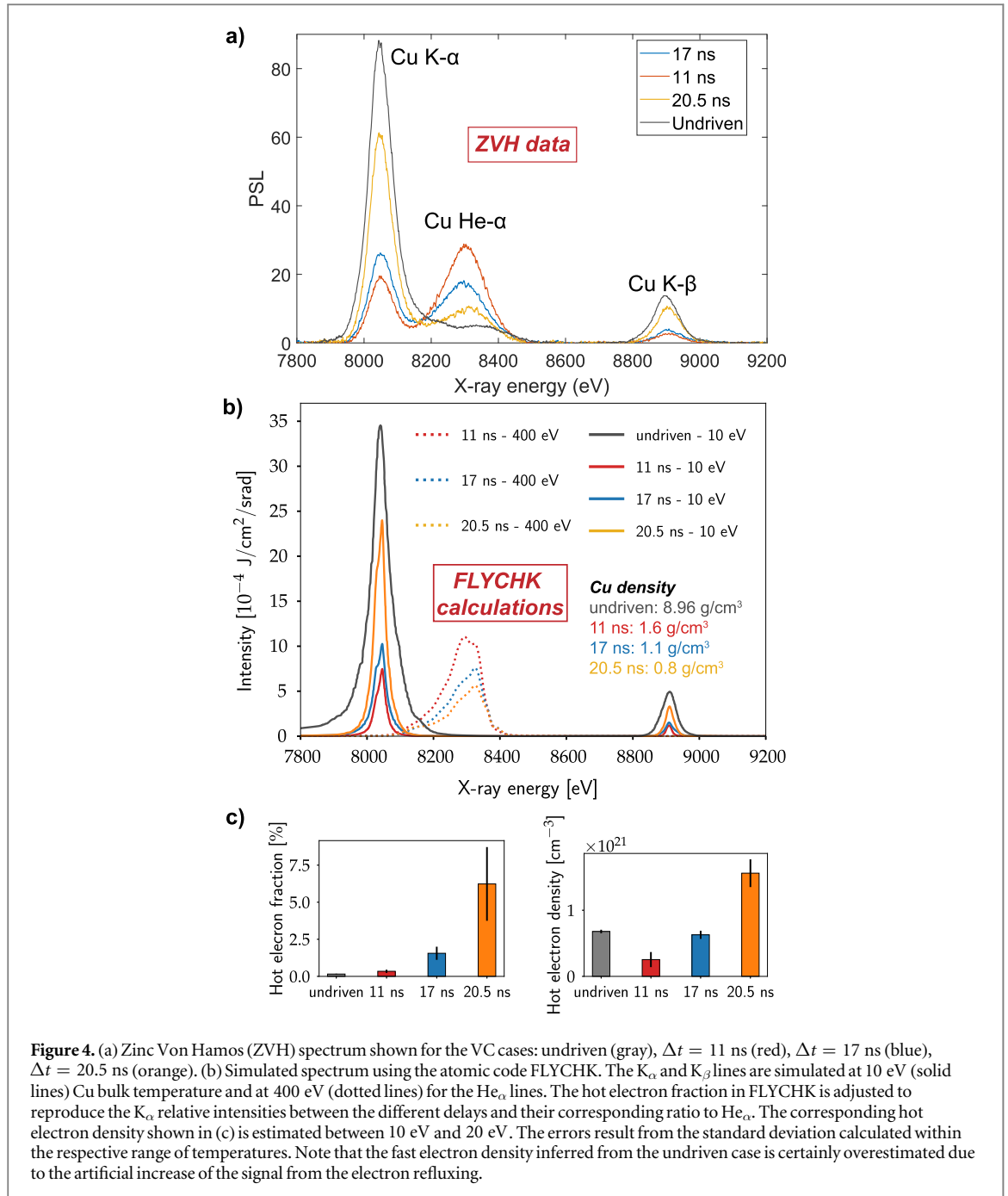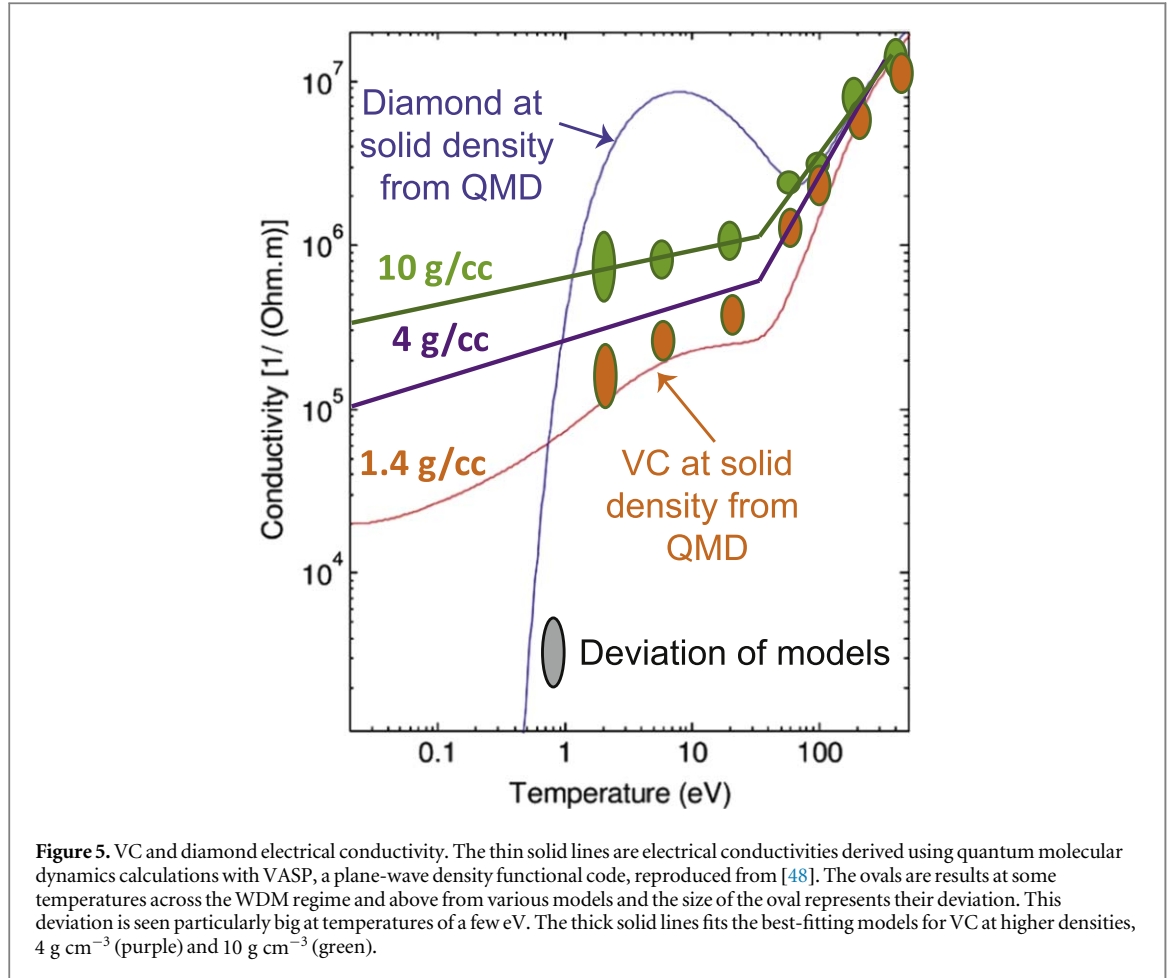
Figure 4. (a) Zinc Von Hamos (ZVH) spectrum shown for the VC cases: undriven (gray), $\Delta t = 11$ ns (red), $\Delta t = 17$ ns (blue), $\Delta t = 20.5$ ns (orange). (b) Simulated spectrum using the atomic code FLYCHK. The K_α and K_β lines are simulated at 10 eV (solid lines) Cu bulk temperature and at 400 eV (dotted lines) for the He$_\alpha$ lines. The hot electron fraction in FLYCHK is adjusted to reproduce the K_α relative intensities between the different delays and their corresponding ratio to He$_\alpha$. The corresponding hot electron density shown in (c) is estimated between 10 eV and 20 eV. The errors result from the standard deviation calculated within the respective range of temperatures. Note that the fast electron density inferred from the undriven case is certainly overestimated due to the artificial increase of the signal from the electron refluxing.

figure 4(c), with the error bar resulting from the uncertainty on the bulk electron temperature within the temperature range. While the absolute value of the hot electron fraction and density rely on the hypothesis of an isochoric evolution of the Cu over the recorded x-ray emission for the 'cold' and 'hot' components, their relative evolution for the different delays (which is of main interest here) could solely be obtained from the K_α lines. It is also worth mentioning that the hot electron fraction and hot electron density inferred from the undriven case is certainly overestimated due to the artificial increase of the signal from the electron refluxing. As discussed previously, the REB energy density coupling is expected to be actually much lower regarding the weak emission of He$_\alpha$.

2.3. Relativistic electron transport modeling

For the validation of experimental results showing a reduced divergence of the fast electrons in shock-heated materials, we performed 2D particle-in-cell (PIC)-hybrid simulations of the REB transport in VC using the target background conditions obtained from hydrodynamic simulations as input for the different delays.

Here we will first discuss on the important role of target resistivity upon fast electron transport with the difficulty it poses in the WDM regime for insulator targets and how we addressed this issue in our REB modeling.

Figure 5. VC and diamond electrical conductivity. The thin solid lines are electrical conductivities derived using quantum molecular dynamics calculations with VASP, a plane-wave density functional code, reproduced from [48]. The ovals are results at some temperatures across the WDM regime and above from various models and the size of the oval represents their deviation. This deviation is seen particularly big at temperatures of a few eV. The thick solid lines fits the best-fitting models for VC at higher densities, 4 g cm^{-3} (purple) and 10 g cm^{-3} (green).

During the fast electron propagation, a return current $\vec{j}_r \approx -\vec{j}_f$ is drawn from the background and nearly cancels the fast electron current. A generalized Ohm law can be derived with the dominant term being $\vec{E} = \eta \vec{j}_r$, η being the background resistivity. It gives rise to an azimuthal magnetic field from Faraday's law that writes:

$$\frac{\partial \vec{B}}{\partial t} = -\vec{\nabla} \times \vec{E} = \eta(\vec{\nabla} \times \vec{j}_f) + (\vec{\nabla}\eta) \times \vec{j}_f. \tag{2}$$

For the majority of time, the first term is a positive, collimating field, which is in competition with the negative, decollimating field of the second term. Note that the second term can also be positive, if the slope of the resistivity/conductivity as a function of temperature is positive/negative. This is for example the case for metals at temperatures below the Fermi temperature of the material (around 10 eV for most materials). This case also includes diamond at solid density for temperatures between 10 and 100 eV. Yet, in the VC cases, the second term is always negative. The resistivity is the main key to decode the divergence and collective effects of a fast electron beam propagating in dense targets with high current densities. For instance, it is relatively trivial, once known the resistivity of VC and diamond at solid density, to qualitatively unravel the undriven transport results (see figure 5). The VC at solid density has a very low electrical conductivity and the fast electron current density gradient is strong along the beam radius. It hence gives rise to unduly strong radially-dependent focusing fields from the first term. Yet, the high target resistivity also triggers resistive filamentation [60, 61]: the beam breaks out into fingers of currents that will eventually make it explode radially. In the case of diamond, the electrical conductivity increases significantly due to the highly-ordered lattice structure with respect to the VC. It relaxes beam hollowing and resistive filamentation instability. Moreover, the positive resistivity gradient (second term) focuses the beam, which helps to build a stable field collimation. The huge difference in resistivity between VC and diamond is therefore responsible of the dramatic change on electron transport reported between VC and diamond undriven cases presented in figure 2. For the REB modeling with insulators such as VC or diamond, resistivity tables or models are not readily available nor benchmarked, as they could be for usual transport medium such as Al. The models are also intrinsically more difficult to develop since the Thomas–Fermi ionization modeling cannot be used for insulators. The absence of data is especially true when studying material conditions departing from solid density in the WDM regime. In figure 5 we report our efforts to model the

electrical conductivity of VC at increasing densities from 1 to 10 g cm^{-3} across the WDM regime. In this figure, the thin orange and blue solid lines are fitted results of Quantum Molecular Dynamics (QMD) calculations with the plane-wave density functional code VASP, reproduced from [48], respectively for VC and diamond at solid density. The ovals represent the conductivity results from various models at temperatures from 2 to 500 eV for solid density and for 10× compressed VC. The size of the ovals indicates the standard deviations of models, which are particularly high below 10 eV. The best-fitting model to QMD results at solid density is used to estimate the conductivity of the compressed VC. Thick solid lines show the trend of the resistivity response of VC at 4 g cm^{-3} (purple) and 10 g cm^{-3} (green). The tables of resistivity are then input in the REB transport code, interpolating the data between 1 and 10 g cm^{-3}.
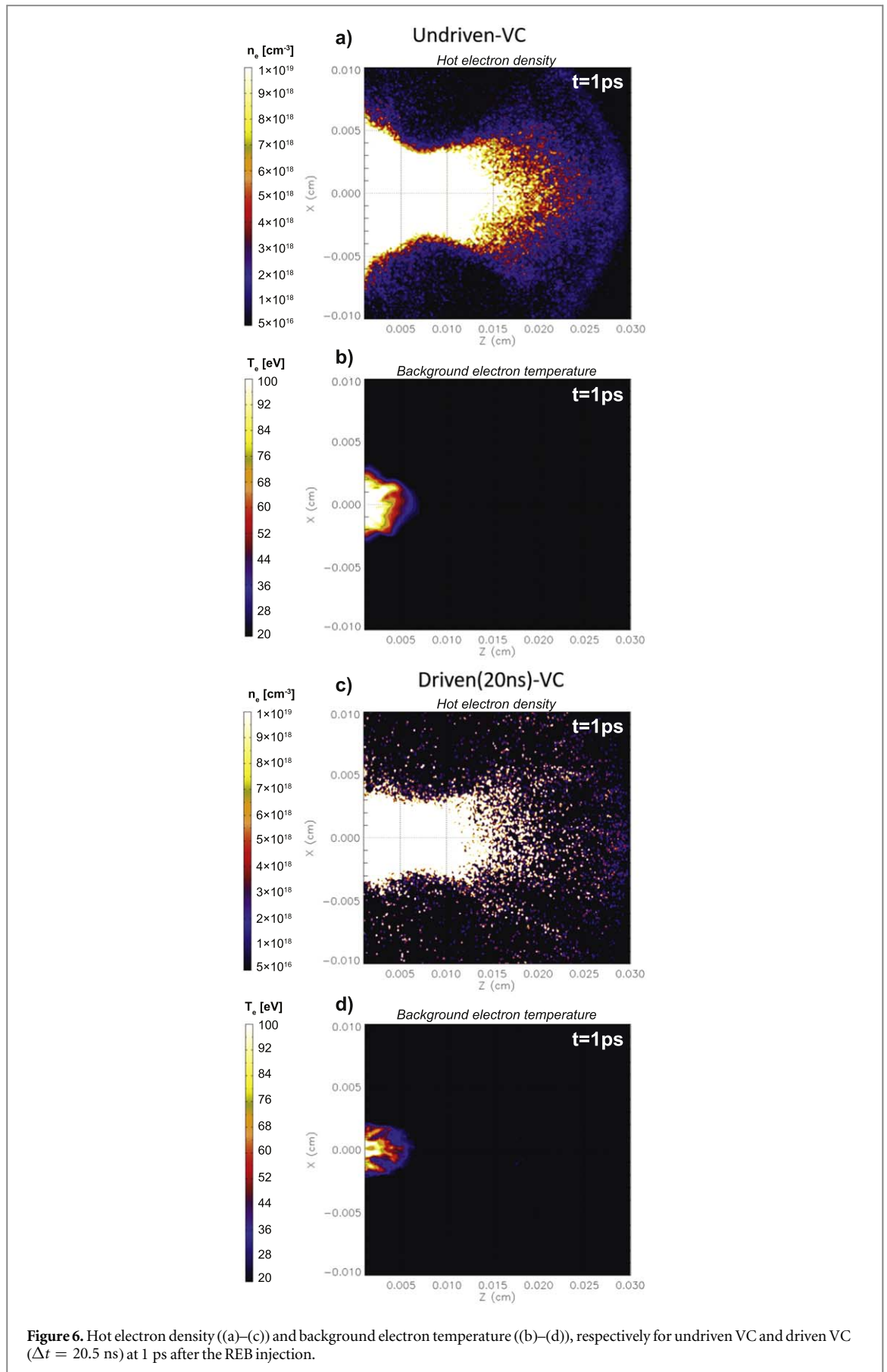
Details of the REB propagation and energy transport are unfolded from 2D Hybrid-PIC simulations with the code LSP, accounting for fast electron collisions with the background material and REB self-generated fields. The initial REB total kinetic energy was set to 30% of the on target SP-laser energy, and injected from the target front-side, within the SP-laser focal spot area (FWHM of 20 μm) and with an initial half-angle divergence of 30° along target axis (normal incidence). The injected electron kinetic energy spectra was characterized by an exponential law $\propto \exp{-E/T_h}$ with $T_h = 2.7$ MeV, as determined by a fit of the electron spectrometer data. The total simulation time was set to 10 ps (with $t = 0$ corresponding to the peak REB flux at the injection plane).

To show the different REB focusing obtained in experiment, we performed simulations of electron transport through 200 μm of undriven diamond (3.5 g cm^{-3}), undriven vitreous carbon (1.4 g cm^{-3}) and driven vitreous carbon (shocked material with a slope of density from 3.8 g cm^{-3} to 0.1 g cm^{-3}).

The resistivity of the cold and warm-dense carbon strongly depends on density and material structure for temperatures below 100 eV (see figure 5). At higher temperatures, dominated by the Spitzer regime, the resistivity mainly depend on background temperature with a $T_e^{3/2}$ slope: the resistivity responses of undriven and driven diamond or VC carbon merges to the same curve. Upon REB injection, the background electron temperature will rise fast to >100 eV. Yet, we evidenced significant differences for the electron transport. A closer look at the edges of the REB in figure 6 shows that they are actually at WDM temperatures. When comparing the hot electron density and background electron temperature for undriven VC (figures 6(a)–(b)) and for driven VC at $\Delta t = 20.5$ ns (figures 6(c)–(d)) at early time ($t = 1$ ps), we can already notice a significant difference in the REB transport for the two cases. The temperature gradients at the edges of the beam are the location of the strong resistive B-field (see next in figure 7) that will impact the beam propagation [49, 54]. Next, we show how it eventually affects the beam at later time (4 ps).

In the first row of figure 7, the fast electron beam density is plot in log-scale. Due to the lower resistivity of diamond, the REB propagate efficiently in the sample with a collimating effect from magnetic field growth, as evidenced by the magnetic field plot shown below. We can note clearly the conduit of resistive B-field at the edges of the beam. In the undriven vitreous carbon case, the beam experiences strong resistive filamentation, as predicted from the high resistivity background at current densities of ∼10^{12} A cm^{-2}. This result is in line with previous work from McKenna *et al* [48]: the ions of vitreous carbon are highly disordered, then bulk electrons scatter incoherently and their mean free path, limited to the mean inter-ionic distance, results in high resistivity. The > kT filaments can be observed in the self-generated magnetic field map drawn on the second row of figure 7. The beam radially explodes and the electron density in the Cu eventually amounts to ∼2 × 10^{19} cm^{-3} at the target rear-side. In contrast, in shock-heated vitreous carbon, the beam is guided along the target axis by a focusing channel of resistive B-field. The lower resistivity of shock-heated vitreous carbon cases limits the beam hollowing and resistive filamentation. Moreover, the defocusing field arising from the gradient of resistivity is also reduced in shock-heated cases (see the $\eta - T$ slope in figure 5). Hence, it forges a stable focusing B-field at the outer radius of the electron beam which efficiently guide it in the target's depth. Eventually, the electron beam density for the shock-driven case amounts to ∼1 − 5 × 10^{20} cm^{-3} which qualitatively agrees with the values inferred from the ZVH analysis in figure 4, with a similar trend.

For a direct comparison with the experimental K$_\alpha$ signal from SCI, we simulated the target sizes of the experiment, then extracted the electron beam parameters at the target rear-side and injected it in Cu with a density profile matching our hydrodynamic simulations. The background density of the transport target is input from the hydrodynamic simulations at the different delays Δt. To mimic the electron refluxing for the undriven case, we used periodic boundary condition at the rear-side of the target, while an open boundary is used for driven cases. The Cu K$_\alpha$ emission is calculated by implementing the fluorescence cross-section into the code. We thereby obtained synthetic K$_\alpha$ distributions in the Cu and radial lineouts are shown in figure 8, to be compared with the experimental lineouts of figure 3(a). The undriven case shows similar large wings emission, which are mainly caused by the electron refluxing, since the electrons recirculate at larger angles. The filamentation also broadens the beam. For driven cases, the emission is much narrower, as observed in the experiment. The synthetic lineout for the undriven case is comparatively lower (respect to driven cases) to what is observed in the experimental data. It may result from an underestimation of the refluxing that would need very long simulation run to be fully accounted for. Nonetheless, the overall comparison of the synthetic profiles to the experiment is
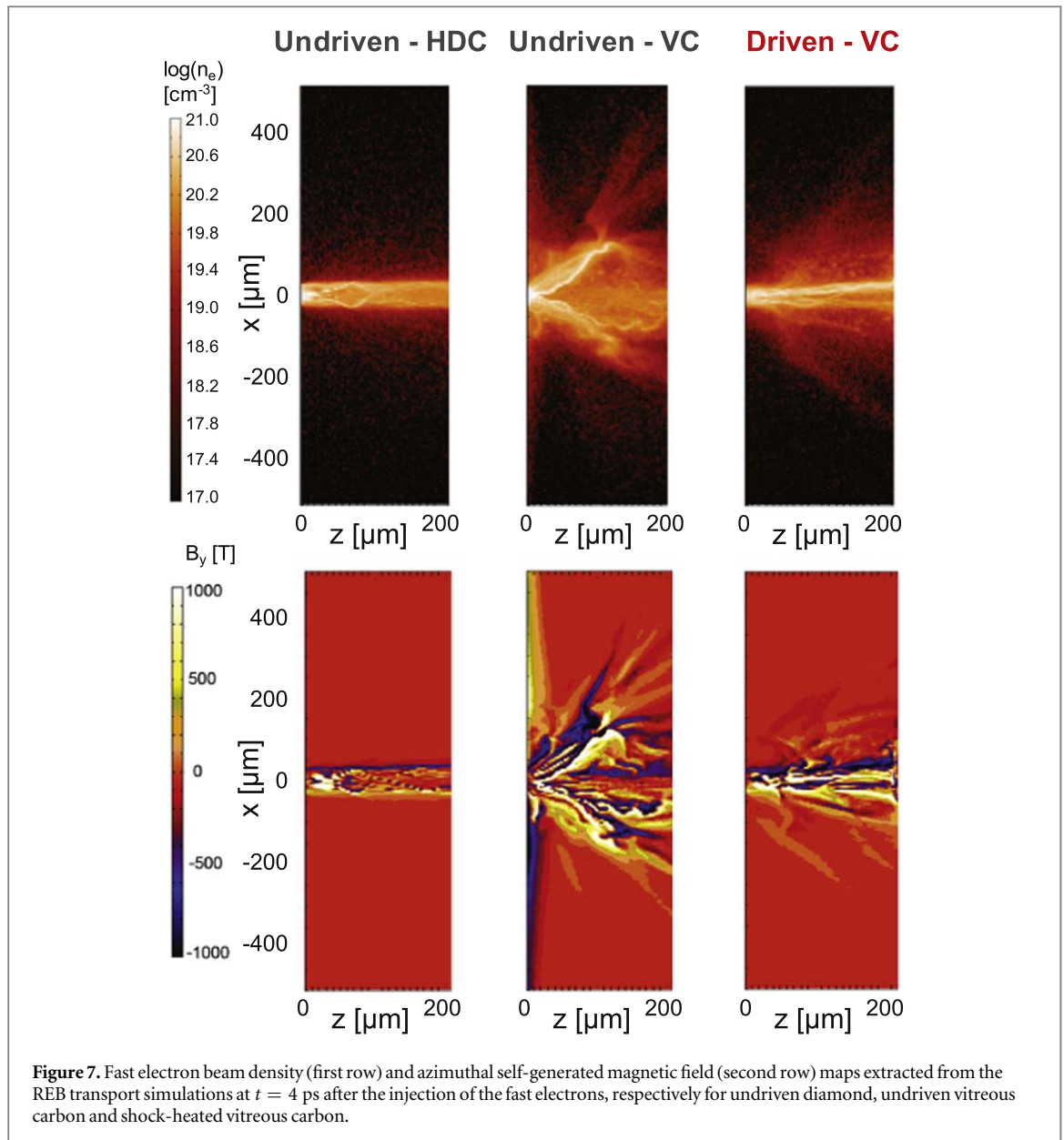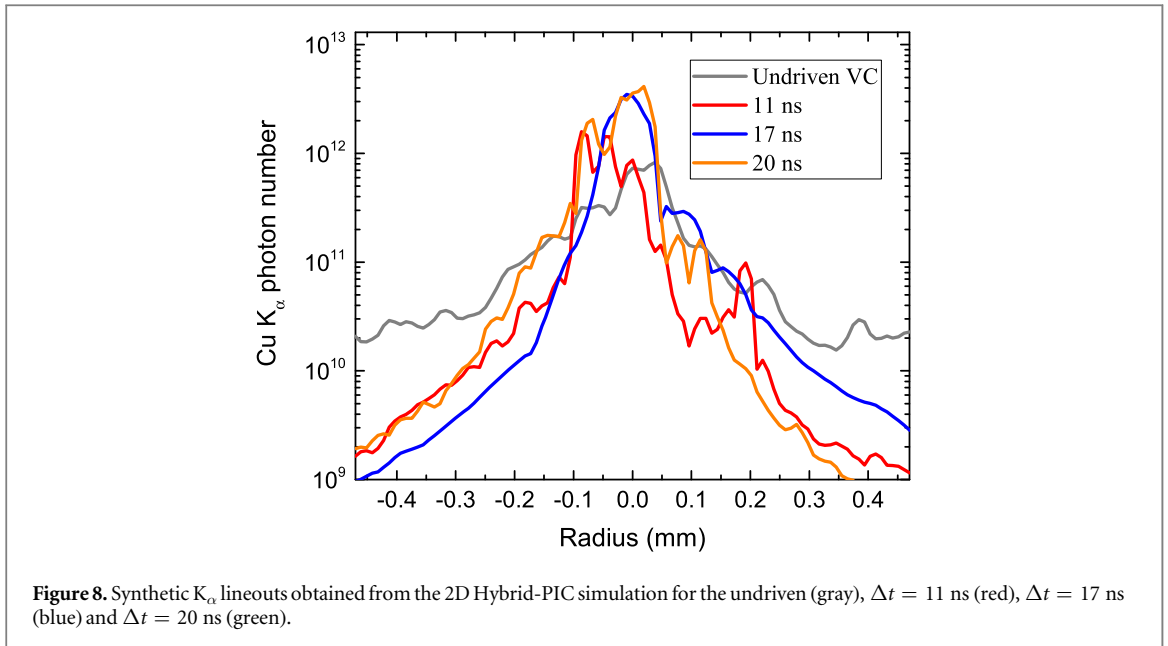
Figure 6. Hot electron density ((a)–(c)) and background electron temperature ((b)–(d)), respectively for undriven VC and driven VC ($\Delta t = 20.5$ ns) at 1 ps after the REB injection.

Figure 7. Fast electron beam density (first row) and azimuthal self-generated magnetic field (second row) maps extracted from the REB transport simulations at $t = 4$ ps after the injection of the fast electrons, respectively for undriven diamond, undriven vitreous carbon and shock-heated vitreous carbon.

fairly conclusive and reveal the role of the background resistivity and associated self-generated fields to explain the increased penetration depth (in equivalent ρL) and the relatively collimated energy transport in shock-heated carbon.

3. Conclusions

In conclusion, we showed the increased guiding of a $\sim$300 J relativistic electron beam over hundreds-of-micron depth in carbon when departing from cold solid density as initial target conditions. While the self-generated fields are triggering resistive filamentation instabilities in cold samples, they help instead to build a stable focusing channel in the shock-heated samples. The electrical resistivity of the target in this highly applicable WDM regime is of paramount importance to explain and reproduce the experimental results and therefore our study provided a useful benchmark and insights for applications of fast-isochoric heating with electrons. In the particular context of laser-fusion research, our study contributes in designing optimized fast electron energy coupling to high-density cores of nuclear fuel. Multi-stage simulations that involve a particular effort on modelling the background resistivity essentially describe the characteristics of the relativistic electron beam transport measurements performed during the experiment. Additional efforts will be needed to input a valid resistivity model into LSP for the diamond cases. However, based on the success of the numerical platform for VC cases, we can now use with confidence our REB modeling to unfold resistivity trends of the shock-heated diamond matching the experimental data. Resistivity models and REB transport modeling in diamond is of

Figure 8. Synthetic K_α lineouts obtained from the 2D Hybrid-PIC simulation for the undriven (gray), $\Delta t = 11$ ns (red), $\Delta t = 17$ ns (blue) and $\Delta t = 20$ ns (green).

timely interest for hot electron transport in the diamond shells used recently in ICF studies for high-adiabat capsule designs [62] . Although the hot electron energies from the long implosion drivers are much lower than in our experiment, their numbers can be important and could impair the ignition if preheating the DT fuel core.

4. Methods

4.1. Hydrodynamic simulations

Hydrodynamic simulations were performed using the Lagrangian multi-material and two-temperatures code CHIC [63], in 2D. The equation of states for vitreous carbon and diamond are taken from the SESAME tables (T7830 for diamond). We extracted the temperature and density maps projected over 350 meshes between -0.02 cm and 0.2 cm along cylinder's height and 250 meshes between 0 and 0.2 cm along cylinder's radius. A zoom over the target area for the density and temperature are given in figure 2 at the differing delays Δt for vitreous and diamond carbon.

4.2. Simulations of relativistic electron beam transport

Electron transport simulations were conducted using the implicit, hybrid, particle-ic-cell code LSP. The simulation domain was 1.3 mm long and 500 μm wide where a carbon target with an initial temperature of 10 eV filled the entire simulation box. Both carbon ions and background electrons were set up as fluid and their charge state was updated by the equation of state tables (PROPACEOS). For different carbon materials, HDC, VC, and compressed VC, the simulations utilized the varying electric conductivity (shown in figure 5) which is based on matter's local thermodynamic states (density and temperature).

The relativistic electrons treated as kinetic species were injected from inside of the carbon target, $z = 0$. Based on the laser parameter in the experiment, the electron beam had a 10 ps temporal duration with 30 μm (FWHM) Gaussian spatial profile. The electron beam, 30% of total laser energy had a Maxwellian energy distribution with a slope temperature of 2.7 MeV which is similar to experimental measurement. For transport of relativistic electrons, scattering and stopping calculation were done using Atzeni's approach [64] in LSP.

In the modeling of experiments, all electron particles that reached the position of the Cu slab were recorded in the extraction planes. From the particle information including numbers and momentum, Cu K_α emission was generated by using the cross-section for electron [65]. To obtain the time-integrated spatial profile of emission, Cu density for each shot case and radiation loss by distance was taken into account.

Acknowledgments

ORCID iDs

M Bailly-Grandvaux ⓘ https://orcid.org/0000-0001-7529-4013
M Dozières ⓘ https://orcid.org/0000-0002-8640-1459
M S Wei ⓘ https://orcid.org/0000-0002-4257-6409
J J Santos ⓘ https://orcid.org/0000-0002-4737-8559
P McKenna ⓘ https://orcid.org/0000-0001-8061-7091
M P Desjarlais ⓘ https://orcid.org/0000-0002-6610-1686
F N Beg ⓘ https://orcid.org/0000-0003-0391-8944

References

[1] Beg F N, Bell A R, Dangor A E, Danson C N, Fews A P, Glinsky M E, Hammel B A, Lee P, Norreys P A and Tatarakis M 1997 A study of picosecond laser-solid interactions up to 10^{19} W cm^{-2} *Phys. Plasmas* **4** 447–57

[2] Wharton K B, Hatchett S P, Wilks S C, Key M H, Moody J D, Yanovsky V, Offenberger A A, Hammel B A, Perry M D and Joshi C 1998 Experimental measurements of hot electrons generated by ultraintense ($>10^{19}$ W cm^{-2}) laser-plasma interactions on solid-density targets *Phys. Rev. Lett.* **81** 822–5

[3] Nilson P M, Theobald W, Myatt J, Stoeckl C, Storm M, Gotchev O V, Zuegel J D, Betti R, Meyerhofer D D and Sangster T C 2008 High-intensity laser-plasma interactions in the refluxing limit *Phys. Plasmas* **15** 056308

[4] Chen C D *et al* 2009 Bremsstrahlung and K$_\alpha$ fluorescence measurements for inferring conversion efficiencies into fast ignition relevant hot electrons *Phys. Plasmas* **16** 082705

[5] Westover B, Chen C D, Patel P K, McLean H and Beg F N 2014 Characterization of the fast electrons distribution produced in a high intensity laser target interaction *Phys. Plasmas* **21** 031212

[6] Macchi A, Borghesi M and Passoni M 2013 Ion acceleration by superintense laser-plasma interaction *Rev. Mod. Phys.* **85** 751–93

[7] Ledingham K and Galster W 2010 Laser-driven particle and photon beams and some applications *New J. Phys.* **12** 45005

[8] Stark D J, Toncian T and Arefiev A V 2016 Enhanced multi-MeV photon emission by a laser-driven electron beam in a self-generated magnetic field *Phys. Rev. Lett.* **116** 185003

[9] Pérez F *et al* 2010 Enhanced isochoric heating from fast electrons produced by high-contrast, relativistic-intensity laser pulses *Phys. Rev. Lett.* **104** 85001

[10] Baton S D *et al* 2007 Relativistic electron transport and confinement within charge-insulated, mass-limited targets *High Energy Density Phys.* **3** 358–64

[11] Nakatsutsumi M *et al* 2008 Heating of solid target in electron refluxing dominated regime with ultra-intense laser *J. Phys.: Conf. Ser.* **112** 022063

[12] Rassuchine J *et al* 2009 Enhanced hot-electron localization and heating in high-contrast ultraintense laser irradiation of microcone targets *Phys. Rev. E* **79** 036408

[13] Morace A *et al* 2009 Study of plasma heating induced by fast electrons *Phys. Plasmas* **16** 122701

[14] Schönlein A *et al* 2016 Generation and characterization of warm dense matter isochorically heated by laser-induced relativistic electrons in a wire target *Europhys. Lett.* **114** 45002

[15] Koenig M *et al* 2010 Simulating earth core using high energy lasers *High Energy Density Phys.* **6** 210–4

[16] Celliers P M *et al* 2004 Electronic conduction in shock-compressed water *Phys. Plasmas* **11** L41–4

[17] Jakubowska K, Batani D, Clerouin J and Siberchicot B 2019 Theoretical and experimental refraction index of shock compressed and pre-compressed water in the megabar pressure range *Europhys. Lett.* **126** 56001

[18] Remington B, Drake R and Ryutov D 2006 Experimental astrophysics with high power lasers and Z pinches *Rev. Mod. Phys.* **78** 755–807

[19] Hoarty D *et al* 2013 Observations of the effect of ionization-potential depression in hot dense plasma *Phys. Rev. Lett.* **110** 265003

[20] Robinson A P L, Strozzi D J, Davies J R, Gremillet L, Honrubia J J, Johzaki T, Kingham R J, Sherlock M and Solodov A A 2014 Theory of fast electron transport for fast ignition *Nucl. Fusion* **54** 54003

[21] Norreys P *et al* 2014 Fast electron energy transport in solid density and compressed plasma *Nucl. Fusion* **54** 54004

[22] Bellei C, Divol L, Kemp A J, Key M H, Larson D J, Strozzi D J, Marinak M M, Tabak M and Patel P K 2013 Fast ignition: dependence of the ignition energy on source and target parameters for particle-in-cell-modelled energy and angular distributions of the fast electrons *Phys. Plasmas* **20** 052704

[23] Freeman R R *et al* 2006 Overview of recent progress in US fast ignition research *J. Phys. IV* **133** 95–100

[24] Volpe L *et al* 2013 Propagation of a short-pulse laser-driven electron beam in matter *Phys. Plasmas* **20** 033105

[25] Pisani F *et al* 2000 Experimental evidence of electric inhibition in fast electron penetration and of electric-field-limited fast electron transport in dense matter *Phys. Rev. E* **62** R5927–30

[26] Tikhonchuk V 2002 Interaction of a beam of fast electrons with solids *Phys. Plasmas* **9** 1416–21

[27] Santos J, Debayle A, Nicolaï P, Tikhonchuk V, Manclossi M, Batani D, Guemnie-Tafo A, Faure J, Malka V and Honrubia J 2007 Fast-electron transport and induced heating in aluminum foils *Phys. Plasmas* **14** 103107

[28] Vauzour B *et al* 2012 Relativistic high-current electron-beam stopping-power characterization in solids and plasmas: collisional versus resistive effects *Phys. Rev. Lett.* **109** 255002

[29] Santos J J *et al* 2002 Fast electron transport in ultraintense laser pulse interaction with solid targets by rear-side self-radiation diagnostics *Phys. Rev. Lett.* **89** 25001

[30] Stephens R *et al* 2004 K$_\alpha$ fluorescence measurement of relativistic electron transport in the context of fast ignition *Phys. Rev. E* **69** 66414

[31] Green J S *et al* 2008 Effect of laser intensity on fast-electron-beam divergence in solid-density plasmas *Phys. Rev. Lett.* **100** 15003

[32] Adam J C, Héron A and Laval G 2006 Dispersion and transport of energetic particles due to the interaction of intense laser pulses with overdense plasmas *Phys. Rev. Lett.* **97** 205006

[33] Debayle A, Honrubia J J, D'Humières E and Tikhonchuk V T 2010 Divergence of laser-driven relativistic electron beams *Phys. Rev. E* **82** 036405

[34] Tabak M, Hammer J, Glinsky M E, Kruer W L, Wilks S C, Woodworth J, Campbell E M, Perry M D and Mason R J 1994 Ignition and high gain with ultrapowerful lasers* *Phys. Plasmas* **1** 1626–34

[35] Shay H, Amendt P, Clark D, Ho D, Key M, Koning J, Marinak M, Strozzi D and Tabak M 2012 Implosion and burn of fast ignition capsules-Calculations with HYDRA *Phys. Plasmas* **19** 92706

[36] Bell A R and Kingham R J 2003 Resistive collimation of electron beams in laser-produced plasmas *Phys. Rev. Lett.* **91** 035003

[37] Leblanc P and Sentoku Y 2014 Scaling of resistive guiding of laser-driven fast-electron currents in solid targets *Phys. Rev. E* **89** 023109

[38] Pérez F *et al* 2011 Magnetically guided fast electrons in cylindrically compressed matter *Phys. Rev. Lett.* **107** 065004

[39] Vauzour B *et al* 2011 Laser-driven cylindrical compression of targets for fast electron transport study in warm and dense plasmas *Phys. Plasmas* **18** 043108

[40] Bailly-Grandvaux M *et al* 2018 Guiding of relativistic electron beams in dense matter by laser-driven magnetostatic fields *Nat. Commun.* **9** 102

[41] Sakata S *et al* 2018 Magnetized fast isochoric laser heating for efficient creation of ultra-high-energy-density states *Nat. Commun.* **9** 3937

[42] Sentoku Y, d'Humières E, Romagnani L, Audebert P and Fuchs J 2011 Dynamic control over mega-ampere electron currents in metals using ionization-driven resistive magnetic fields *Phys. Rev. Lett.* **107** 135005

[43] Chawla S *et al* 2013 Effect of target material on fast-electron transport and resistive collimation *Phys. Rev. Lett.* **110** 025001

[44] Chawla S, Bailly-Grandvaux M, McLean H S, Patel P K, Wei M S and Beg F N 2019 Effect of target material on relativistic electron beam transport *Phys. Plasmas* **26** 033111

[45] Robinson A P L, Key M H and Tabak M 2012 Focusing of relativistic electrons in dense plasma using a resistivity-gradient-generated magnetic switchyard *Phys. Rev. Lett.* **108** 125004

[46] Schmitz H, Lloyd R and Evans R G 2012 Collisional particle-in-cell modelling of the generation and control of relativistic electron beams produced by ultra-intense laser pulses *Plasma Phys. Control. Fusion* **54** 85016

[47] Debayle A, Gremillet L, Honrubia J and D'Humières E 2013 Reduction of the fast electron angular dispersion by means of varying-resistivity structured targets *Phys. Plasmas* **20** 13109

[48] McKenna P *et al* 2011 Effect of lattice structure on energetic electron transport in solids irradiated by ultraintense laser pulses *Phys. Rev. Lett.* **106** 185004

[49] MacLellan D A *et al* 2013 Annular fast electron transport in silicon arising from low-temperature resistivity *Phys. Rev. Lett.* **111** 095001

[50] Vauzour B *et al* 2014 Unraveling resistive versus collisional contributions to relativistic electron beam stopping power in cold-solid and in warm-dense plasmas *Phys. Plasmas* **21** 33101

[51] Vaisseau X *et al* 2015 Enhanced relativistic-electron-beam energy loss in warm dense aluminum *Phys. Rev. Lett.* **114** 095004

[52] Hall T A *et al* 1998 Fast electron deposition in laser shock compressed plastic targets *Phys. Rev. Lett.* **81** 1003–6

[53] Batani D *et al* 2000 Explanations for the observed increase in fast electron penetration in laser shock compressed materials *Phys. Rev. E* **61** 5725–33

[54] Vaisseau X *et al* 2017 Collimated propagation of fast electron beams accelerated by high-contrast laser pulses in highly resistive shocked carbon *Phys. Rev. Lett.* **118** 205001

[55] Jarrott L C *et al* 2017 Calibration and characterization of a highly efficient spectrometer in von Hamos geometry for 7–10 keV x-rays *Rev. Sci. Instrum.* **88** 043110

[56] Habara H, Iwawaki T, Gong T, Wei M S, Ivancic S T, Theobald W, Krauland C M, Zhang S, Fiksel G and Tanaka K A 2019 A ten-inch manipulator (TIM) based fast-electron spectrometer with multiple viewing angles (OU-ESM) *Rev. Sci. Instrum.* **90** 063501

[57] Stoeckl C, Fiksel G, Guy D, Mileham C, Nilson P M, Sangster T C, Shoup M J and Theobald W 2012 A spherical crystal imager for OMEGA EP *Rev. Sci. Instrum.* **83** 033107

[58] Neumayer P *et al* 2010 The role of hot electron refluxing in laser-generated K-alpha sources *Phys. Plasmas* **17** 103103

[59] Chen M, Sheng Z-M and Zhang J 2006 On the angular distribution of fast electrons generated in intense laser interaction with solid targets *Phys. Plasmas* **13** 014504

[60] Gremillet L, Bonnaud G and Amiranoff F 2002 Filamented transport of laser-generated relativistic electrons penetrating a solid target *Phys. Plasmas* **9** 941–8

[61] McKenna P, MacLellan D A, Butler N M H, Dance R J, Gray R J, Robinson A P L, Neely D and Desjarlais M P 2015 Influence of low-temperature resistivity on fast electron transport in solids: scaling to fast ignition electron beam parameters *Plasma Phys. Control. Fusion* **57** 064001

[62] Casey D T *et al* 2018 The high velocity, high adiabat, 'Bigfoot' campaign and tests of indirect-drive implosion scaling *Phys. Plasmas* **25** 056308

[63] Breil J, Galera S and Maire P-H 2011 Multi-material ale computation in inertial confinement fusion code chic *10th ICFD Conf. Series on Numerical Methods for Fluid Dynamics (ICFD 2010); Comput. Fluids* **46** 161–7

[64] Atzeni S, Schiavi A and Davies J R 2009 Stopping and scattering of relativistic electron beams in dense plasmas and requirements for fast ignition *Plasma Phys. Control. Fusion* **51** 015016

[65] Hombourger C 1998 An empirical expression for K-shell ionization cross section by electron impact *J. Phys. B: At. Mol. Phys.* **31** 3693–702